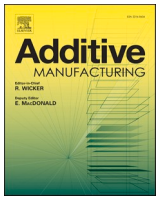
Additive Manufacturing 74 (2023) 103712



Contents lists available at ScienceDirect

Additive Manufacturing

journal homepage: www.elsevier.com/locate/addma



Research paper

Refinement of Ti-6Al-4V prior-β grain structure in the as-deposited condition via process control during wire-direct energy deposition

James Wainwright *, Stewart Williams, Jialuo Ding

Welding Engineering and Laser Processing Centre, Cranfield University, Bedfordshire MK43 0PL, United Kingdom

ARTICLE INFO

Keywords:
Ti-6Al-4V
Additive manufacturing
Grain refinement
Columnar-to-equiaxed transition
As-deposited

ABSTRACT

This study demonstrates that refinement of the prior-β grains generated during the wire-direct energy deposition of Ti-6Al-4V is achievable whilst maintaining a stable processing condition in the as-deposited condition, not reliant on penetration of the feedstock to the melt pool. Previous studies on prior-β grain refinement of Ti-6Al-4V have been reliant on either post-processing, alloy modification or agitation of the melt pool to achieve refinement. Through process control alone, it was identified that an increase in the deposition rate for a fixed energy input led to a reduction in the specific energy density of deposited material. Utilising pyrometry, it was determined that the reduction in the specific energy density led to a decrease in the thermal gradient, measured using a linear thermal gradient approximation, encouraging apparent homogenous nucleation within the melt pool. Whilst maintaining a stable 'droplet' transfer mode, the gradual reduction in specific energy density transformed the grain structure from the typical columnar morphology through a mixed morphology to an equiaxed grain morphology; confirmed via prior-β grain reconstructions and inverse pole figure analysis made possible by electron back scattered diffraction microscopy of the deposited samples. Microhardness measurements demonstrated larger variations in the refined prior-β grain specimens as compared to the columnar as a result of more complex α morphologies generated.

1. Introduction

Additive Manufacturing (AM) is a technique used to create near-net shape components through the successive layer-by-layer deposition of a feedstock material. Typically, such near-net shape components require little or no post-processing [1]. Several distinct AM processes exist, each having unique benefits and drawbacks. They are characterized by feedstock and energy source, therefore, labelled a wire or powder-based process using an arc, laser or electron beam heat source, or, some combination to form a hybrid process. One such process is Wire + Arc Additive Manufacturing (WAAM), which has the potential to rival conventional forgings [1,2]. WAAM is a direct energy deposition (DED) process where a wire feedstock is fed directly into an electric arc heat source attached either to a CNC gantry or robotic manipulator in overlapping weld deposits to form a single homogenous component. This process produces significantly reduced material wastage when compared to the traditional substrative manufacturing of a billet, whilst providing comparable mechanical properties [2–5]. However, the deposition is best described as a preform which typically requires some element of machining before service [6].

WAAM flourishes in the manufacturing of medium to large scale components, benefiting from a low capital investment requirement and readily available welding wire feedstock [2,7,8]. It is possible to deposit most types of material, from common metallics such as steel and aluminium to refractory metals such as tungsten and molybdenum [2,9]. WAAM is applicable to the deposition of titanium alloy preforms, particularly Ti-6Al-4V, a common place material in the aerospace industry within airframe and aeroengine applications due to its high specific strength, corrosion resistance and electromechanical compatibility with composites. WAAM is ideally suited for the creation of titanium components, due to the cost of extraction, processing and machineability of titanium [10] by reducing the typical buy-to-fly ratio of 10–20 to < 1.5 and reducing manufacturing lead times from months to mere hours [2]. However, limitations do exist, WAAM processes suffer from high heat accumulation leading to complex thermal histories and residual stresses that effect grain structure and mechanical properties [11,12]. Additionally, titanium has high chemical affinity with oxygen, requiring the use of local or global shielding devices to avoid

* Corresponding author.
E-mail address: j.c.wainwright@cranfield.ac.uk (J. Wainwright).

https://doi.org/10.1016/j.addma.2023.103712
Received 4 April 2023; Received in revised form 23 July 2023; Accepted 28 July 2023
Available online 1 August 2023
2214-8604/© 2023 The Authors. Published by Elsevier B.V. This is an open access article under the CC BY license (http://creativecommons.org/licenses/by/4.0/).

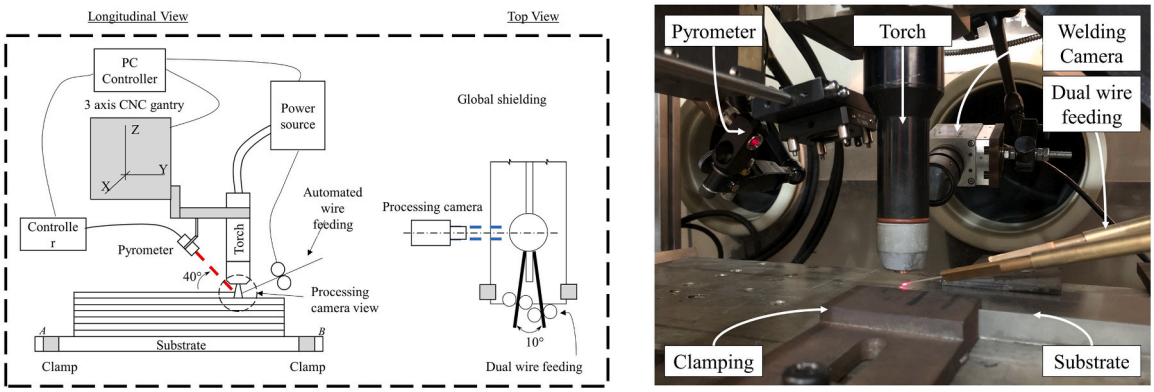


Fig. 1. (L) Schematic of experimental setup. (R) Experimental Setup.

Table 1
Wire feedstock composition Ti-6Al-4V (wt%).

O	N	C	Fe	Al	V	Si	H	Ti
0.15	0.008	0.021	0.18	6.14	3.94	0.012	0.0004	BAL

Table 2
Deposition parameters.

ID	Voltage (V)	Current (A)	Travel Speed (mm/s)	Total WFS (mm/s)	SED ($J.mm^{-3}$)
1	18.41	103.57	4.00	26.67	37.93
2	18.74	103.52	4.00	33.87	30.39
3	19.07	103.21	4.00	36.67	28.48
4	18.79	104.29	4.00	46.67	22.28
5	19.81	102.95	4.00	50.00	21.64

embrittlement known as alpha case hardening that impacts ductility and crack initiation properties, particularly at the outer surface [13,14].

A major limitation of Ti-6Al-4V WAAM components is the epitaxially developed prior-β grain structure in the as-deposited condition in which a coarse textured columnar grain structure is present, typically extending from the bottom to the top of the deposit [15], resulting in significant mechanical anisotropy and fatigue behaviour[16–21]. To refine this unavoidable columnar grain structure of Ti-6Al-4V requires the promotion of nucleation ahead of the solidification front i.e. homogenous nucleation, which for Ti-6Al-4V process control is typically avoided due to the innate lack of favourable solidification conditions. Instead, investigators have typically focused on external forms of manipulation including alloy modification, melt pool agitation and mechanical processing.

Alloy modification can be used to alter the chemical composition of the deposit to refine grains in several ways. Nucleation ahead of the solidification front can be promoted through the introduction of

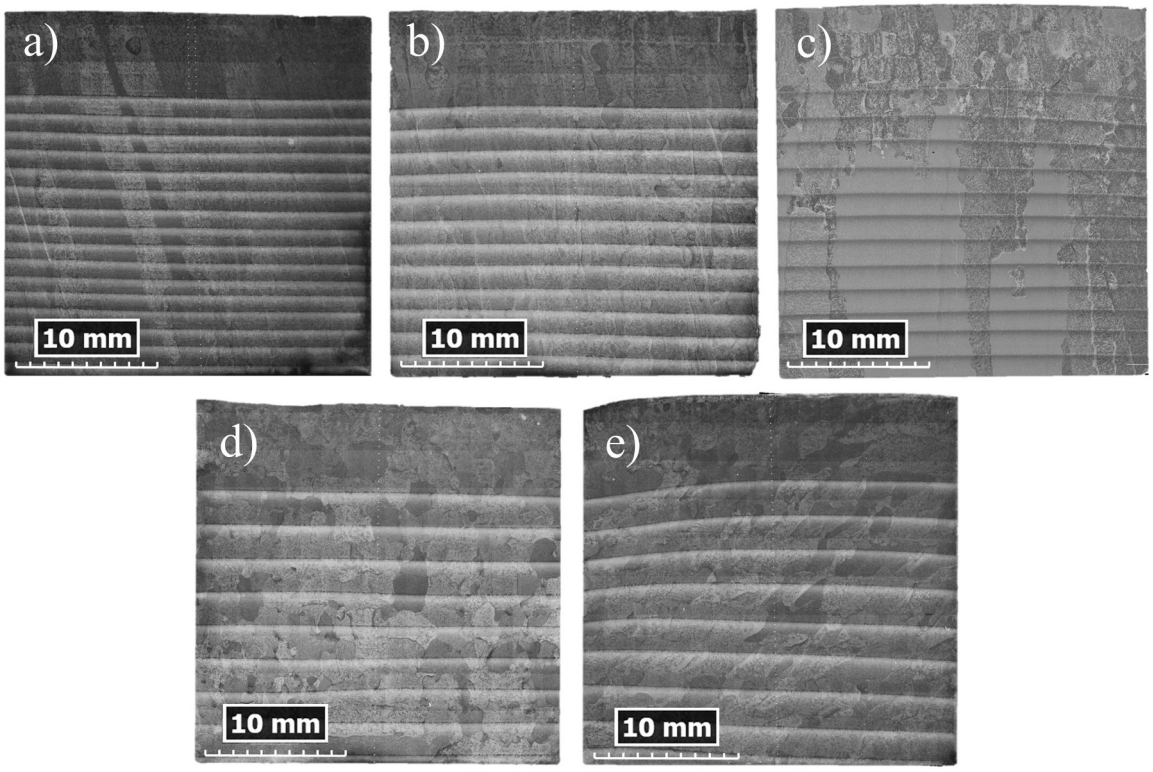


Fig. 2. Etched macrographs of Ti-6Al-4V specimens 1–5 illustrating change in prior-β grain morphology changes as SED of deposited material is reduced a) 37.93 J.mm^{-3}, b) 30.39 J.mm^{-3}, c) 28.48 J.mm^{-3}, d) 22.28 J.mm^{-3}, e) 21.64 J.mm^{-3}.

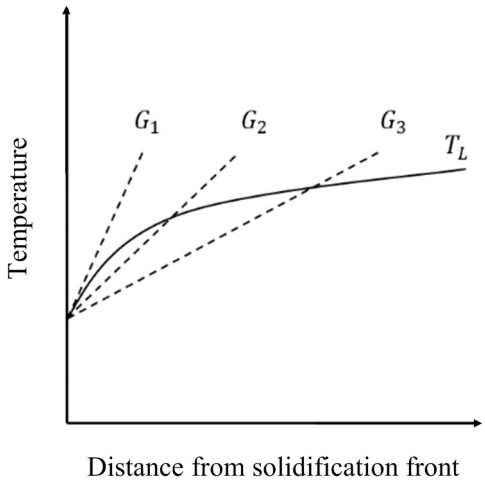


Fig. 3. Illustration outlining the effect of how a reduction in thermal gradient increases the total amount of undercooling by increasing the total area created by the liquidus temperature line (T_L) and dashed thermal gradient line. *Note that here the curvature of T_L does not represent Ti-6Al-4V and is inflated for the purpose of explanation.

elements that provide greater solute partitioning, thus constitutional supercooling. The alteration of the feedstock material to include such elements to alter the liquidus temperature, increases the size of the 'mushy' zone, encouraging competitive dendritic growth in the segregated compositionally rich solute. The introduction of growth restricting elements such as boron [22] prevents already nucleated grains from growing further, limiting their size and encouraging competitive dendritic growth. The inoculation of the melt pool by introducing foreign particles or elements [20], which in addition to increasing the size of the 'mushy' zone, act as nucleation sites for competitive growth. Whilst alloy modification has been successful in refinement of grains, highlighting the importance of increasing the constitutional supercooling, it can lead to the deposition of 'dirty' alloys, where these trace elements have a high probability to form detrimental secondary phases, limiting application [20,23] or may alter primary microstructural and mechanical characteristics. Typically, the methods used to achieve inoculation are uncontrollable and rely on blowing powder into the melt pool or introducing a particle infused sticky residue pre-deposition to the previously deposited layer [20]. Refinement by alloy modification may occur via development of new wire compositions, however, this is expensive.

Ultrasonic agitation of the melt pool has demonstrated success in refining the columnar prior-β grain structure in powder processes. The vibration induces acoustic cavitation inside the melt pool activating nuclei [24] and triggering dendrite fragmentation [25] leading to the development of an equiaxed grain structure, whereby new nuclei and fragmented dendrites impede the growth of epitaxially grown grains and thus formation of a columnar prior-β grain structure. However, this method of refinement requires high frequency vibration. In powder processes or deposition of 'small' components this is feasible, for applicability to large-scale WAAM components that may weigh upwards of tens of kilograms, this method does not appear practically replicable and is yet to be demonstrated successfully.

Mechanical processing of WAAM components is currently the most feasible and widely researched method of grain structure control in titanium alloys. The introduction of a plastic strain to a deposit post-solidification provides β grains the opportunity to recrystallize upon the subsequent heating cycle of the successive layer being deposited. The most common methods for mechanical processing of titanium alloys are rolling [18] and machine hammer peening [21,26], with new processes such as in-situ 'hot-forging' being developed that may become applicable to titanium alloy systems [27,28]. The effectiveness of mechanical postprocessing is substantial, however, can lead to an outer skin of non-refined grains with only the central bulk of material being refined, usually this is less prevalent with rolling than peening [19]. The major limitations of this method include the reduced complexity of deposition features to allow access for the rolling or peening tool to effectively refine the grain structure and the requirement of large scale machinery for rolling. In both cases the additional post-processing leads to a reduction in productivity.

All described methods provide metallurgical and processing clues for the requirements of achieving refinement i.e. constitutional supercooling and recrystallisation, however, translation into direct process control, i.e. a method based upon the manipulation of the process parameters, has demonstrated little success in refining the prior-β grain structure of Ti-6Al-4V in the as-deposited condition. The current refinement techniques add constraints on part design and freedom, incurring greater capital cost and lead time, and are counterproductive and contrary to the ethos of WAAM [2].

This paper demonstrates a new and novel approach to produce a refined prior-β grain structure and weakening of texture in the deposition of Ti-6Al-4V by WAAM and understanding of the α phase microstructural effects through prior-β grain structure control in the as-deposited condition, giving greater design flexibility, localization of grain structure (and by extension mechanical properties), without introducing further capital cost or lead time.

2. Theory

Classical solidification theory suggests that to achieve the columnar

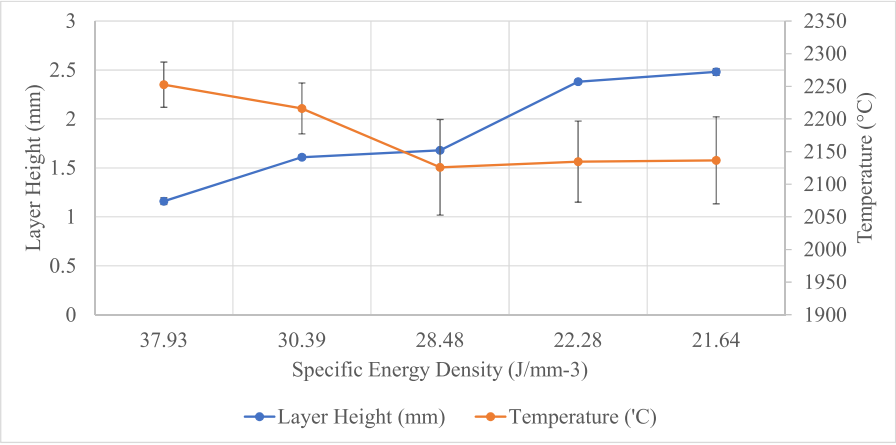


Fig. 4. Effect of SED on layer height and recorded temperature during deposition.

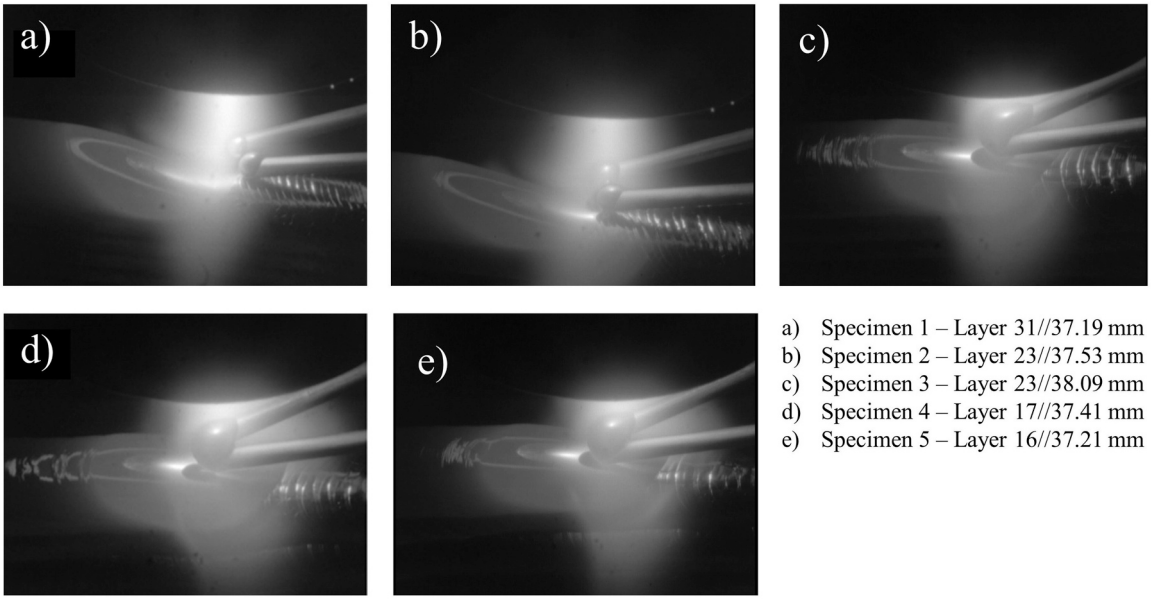


Fig. 5. Droplet transfer mode during deposition. a) 37.39 J.mm^{-3} – TM2, b) 30.39 J.mm^{-3} – TM2, c) 28.48 J.mm^{-3} – TM3, d) 22.28 J.mm^{-3} – TM3, e) 21.64 J.mm^{-3} – TM3 at ~ 38 mm build height.

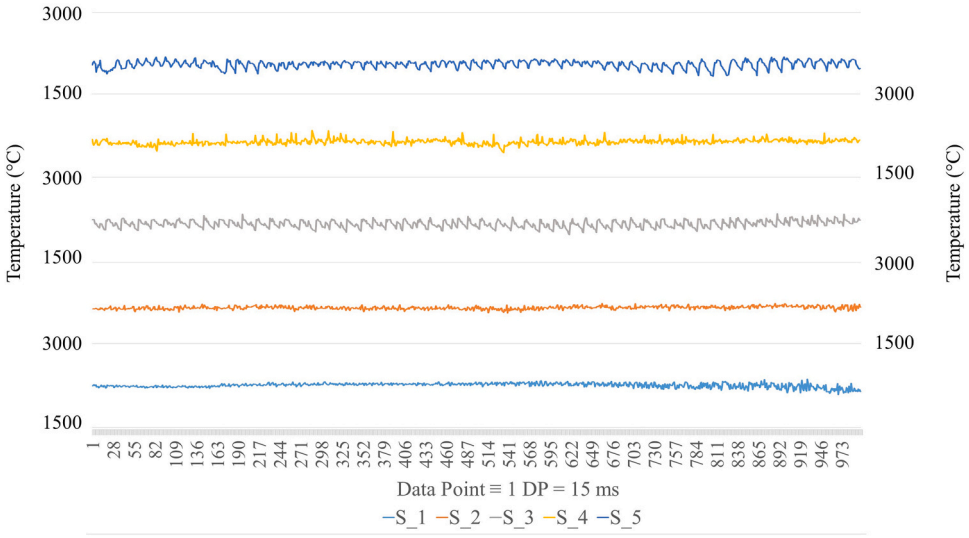


Fig. 6. Real-time pyrometric recording for specimens 1–5 (ascending). (15 ms interval time per data point.) Specimen layers: 31, 23, 23, 17, 16 respective to Fig. 5 observed transfer modes.

to equiaxed transition i.e. grain refinement, it essential for supercooled solute to exist ahead of the solidification front to allow equiaxed grains to form via homogenous nucleation and/or survival and growth of fragmented dendrites within the melt pool. Additionally, this requires either a reduction in the thermal gradient or an increase in the solidification velocity [22,24,29–32] to promote nucleation. The thermal gradient is responsible for defining the morphology of the solidification as either planer, cellular or dendritic dependent on its value [33]. During WAAM, a dendritic solidification front exists, where dendrites grow opposite to the heat flux i.e. from the substrate into the melt pool [34]. The solidification velocity has an effect on the amount of constitutional supercooling at the solidification front, with an increase causing compression of the solute rejection and increased cooling rate, preventing nuclei remelting thus increasing their survival rate [29].

An attempt to increase the solidification velocity by increasing the travel speed (TS) during deposition demonstrated that a mixed grain structure was obtainable [30]. The resulting prior-β grain structure comprised of distinctly columnar grains, however, a mixture of smaller and medium-sized refined grains proved obtainable along the columnar grain boundaries. Using a pyrometer to measure the melt pool temperature during deposition, Bermingham et al. [30] were able to retrospectively calculate a simplified thermal gradient, based upon a linear thermal gradient approximation and rectangular melt pool shape with the layer height and solidification temperature known. This enabled the prediction of grain structures in agreement with the solidification map presented by Kobryn and Semiatin [32]. The mixed grain structure should not be unexpected due to the decrease in the wire feed speed/-travel speed (WFS/TS) ratio as TS increased. It has been demonstrated elsewhere that a decrease in the WFS/TS ratio reduces the layer height [35]. Therefore, increasing the solidification velocity by means of the travel speed is not efficient at refining grain structure as this incurs an increase in the thermal gradient during solidification, hence the mixed

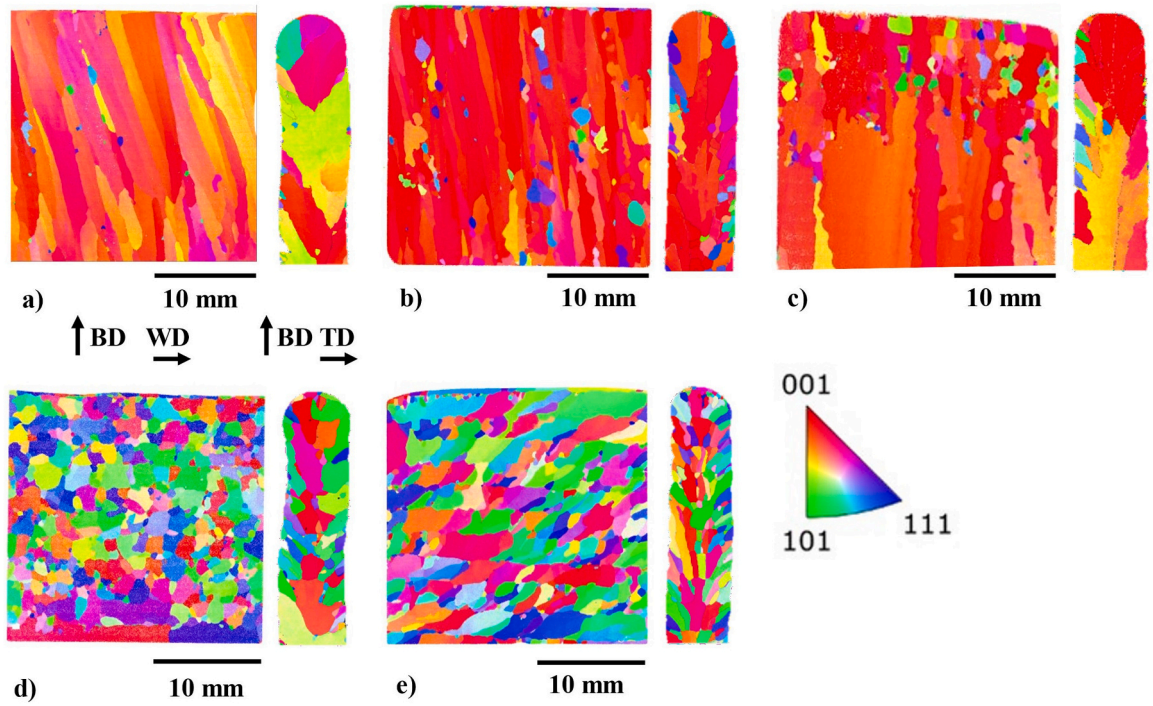


Fig. 7. EBSD IPF maps of specimens 1–5 with reducing SED, a) 37.93 J.mm^{-3}, b) 30.39 J.mm^{-3}, c) 28.48 J.mm^{-3}, d) 22.28 J.mm^{-3} e) 21.64 J.mm^{-3}, showing the transition from a columnar grain structure to a refined one in both the longitudinal and transverse plane.

grain structure.

Resistive heating of the feedstock wire to enable a reduction in the arc current has been shown to successfully refine prior-β grains [36]. The underlying mechanism is attributed to a reduction in the thermal gradient that is obtained in the melt pool as the arc heat input is reduced with increasing resistive heating current. The methodology requires the feedstock to be fed directly into the melt pool to complete a resistive heating circuit, the larger the resistive current the lower the arc current required. It can be observed that the overall energy input to the deposit is decreasing as there is a notable decrease in width and increase in layer height. Using the simplified method detailed by Bermingham et al. [30], a reduction in thermal gradient would be observed and at face-value the reason for refinement. However, by penetrating the melt pool with the feedstock there would be significant melt pool agitation and the introduction of a negative thermal gradient at the contact point (where the temperature of the un-melted wire is lower than the melt pool temperature) and likely dendritic fragmentation. Therefore, the mechanism of refinement cannot be explicitly determined. Additionally, due to innate process fluctuations, in order to maintain continuous penetration of the melt pool is difficult and considered unstable [37], there is the possibility for numerous process defects such as lack of fusion, spatter and misalignment of the wire feedstock.

A study by Wang et al. [38] demonstrated the ability to deposit a localized grain structure. Through the variation of WFS for a fixed heat input, a columnar to fully equiaxed specimen was deposited. The mechanism behind the refinement is still unclear. It was surmised that there is a reduction in the thermal gradient as the increased volume of wire cools the melt pool and similarly relies on the wire entering the melt pool to generate a negative thermal gradient to block epitaxial growth. This appeared in a similar study by Wang et al. [39] which demonstrated the same level of refinement through deliberately forcing the feedstock to penetrate the melt pool. Wang et al. [39] argued that a localized negative thermal gradient acts as a nucleation front at the top of the melt pool, with additional agitation to activate nuclei and dendrite fragmentation also responsible. However, reliance on this process condition does not provide a stable process and is not applicable in all methods of deposition, and ultimately this type of transfer mode is generally avoided as it can lead to numerous potential defects [37].

Whilst these studies have shown evidence of success, questions remain on the mechanism of refinement and their reliability. Studies that show refinement without a reliance on melt pool agitation were unable to deposit a fully refined structure although previous studies indicate that the total energy supplied during deposition influences the grain structure achieved. Hence, to deposit a refined prior-β grain structure in Ti-6Al-4V via control of processing conditions whilst maintaining a stable process condition without melt pool agitation, a new parameter, the specific energy density of deposited material (SED), detailed in Eq. 1, is proposed.

$$SED \quad \left(J.mm^{-3}\right) = \frac{4\eta VI}{WFS * \pi d^2} \tag{1}$$

Eq. 1 compiles the basic deposition parameters (where **η** represents the process efficiency taken from BS EN 1011–1:2009 for plasma arc welding, **V** and **I** represent arc voltage and current, **WFS**, the wire feed speed and **d** the wire feedstock diameter) and can be easily manipulated via the WFS. The expected outcome is that as SED is reduced, the total energy is shared across a larger volume of deposited material, reducing the overall melt pool temperature and thus thermal gradient. A significant reduction in the thermal gradient will drive homogenous nucleation and trigger grain refinement. The SED represents the total energy delivered to and shared by the feedstock material and is not to be confused with the heat input (HI), which measures the total energy delivered to the substrate. In this study the total heat input, measured by Eq. 2 (where **TS** represents the travel speed of the torch), does not change as the arc energy and travel speed remain constant.

$$HI \quad \left(J.mm^{-1}\right) = \frac{\eta VI}{TS} \tag{2}$$

3. Methodology

In this study a total of five samples were deposited on individual Ti-6Al-4V substrates (175 mm x 50 mm x 10 mm) clamped to an

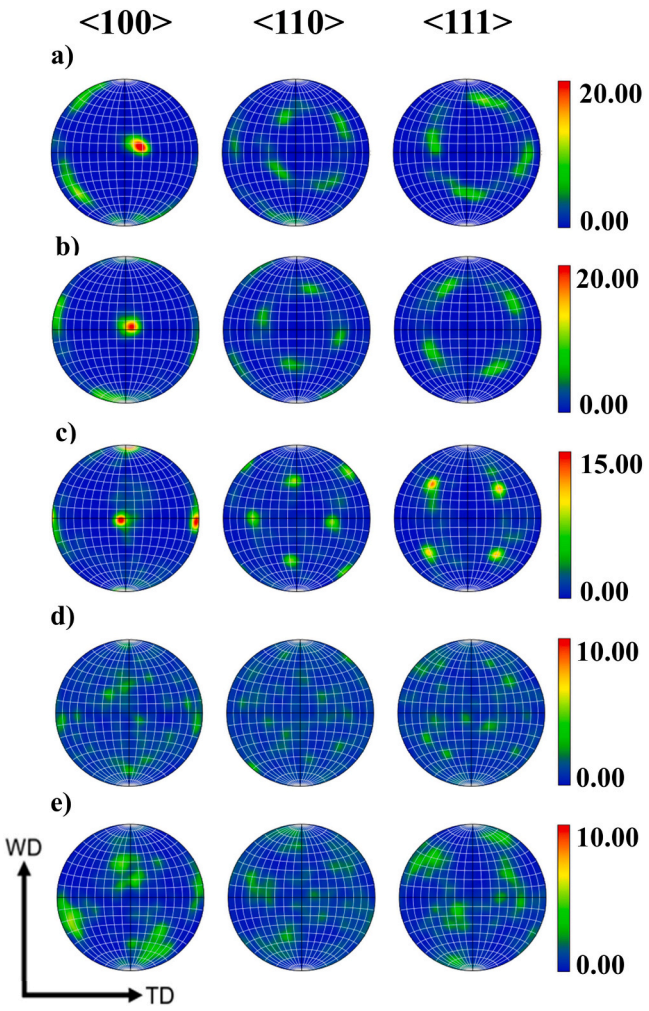


Fig. 8. Pole figures of specimens 1–5 indicating crystallographic texture a) 37.93 J.mm^{-3} b) 30.39 J.mm^{-3}, c) 28.48 J.mm^{-3}, d) 22.28 J.mm^{-3}, e) 21.64 J.mm^{-3}.

Table 3
Effect of SED on average grain size and aspect ratio.

Specimen	SED (J.mm^{-3})	Number of grains	Mean grain size (μm)	Mean aspect ratio
1	37.93	96	1797 ± 220	3.94 ± 0.26
2	30.39	313	1147 ± 64	3.69 ± 0.16
3	28.48	444	942 ± 46	2.33 ± 0.07
4	22.28	710	821 ± 23	1.83 ± 0.03
5	21.64	532	973 ± 34	2.47 ± 0.07

aluminium backing plate at all four corners. A PWP Viper MC plasma torch was coupled to a TECARC PLASWELD 400 DC power source and used to deposit 150 mm long deposits. Two Migatronic KT4 wire feeders were front-fed into the center of the arc, at identical WFS, to feed 1.2 mm diameter Ti-6Al-4V wire feedstock with a 10° offset. All samples were deposited inside a globally shielded environment purged with UN1006 Pureshield Argon to maintain an oxygen level of < 100 PPM monitored by a Argweld PurgEye 600. A schematic of the experimental setup is illustrated in Fig. 1. The wire feedstock composition is provided by the manufacturer (Perryman) subject to their quality assurance methods at the time of production in Table 1.

A single pass, single direction deposition strategy was utilized, controlled via a CNC gantry. In all cases a minimum of 20 mm was first deposited to account for conduction losses through the substrate. This effect is present during the initial layers of a deposit due to the high heat extraction rate from the substrate material, drawing heat away by conduction and is indicated by the stability of the bead geometry in terms of width and height. A further 30 mm of material was deposited for microstructural analysis. During deposition all layers were cooled to < 40 ℃ aided by a cooling line containing UN1006 Pureshield Argon after a single minute of ambient cooling. This removed variability in pre-deposition temperature as the thermal mass changed with the addition of each deposited layer, a pre-defined cooling time would not account for this and would lead to inconsistency between the deposition start and end point.

All processing parameters were kept constant with the exception of combined WFS, manipulated to achieve the desired SED. The WFS's chosen for this study were determined from SED calculated from the study by Wang et al. [38]. Table 2 indicates the parameters used in this study.

A Sensortherm Metis M311 2-colour pyrometer was used to measure the melt pool temperature with the spot center 2 mm behind the arc center at an angle of 40° from the substrate at a focal length of 120 mm and 15 ms response time. This point was selected as the closest point to the center of the melt pool (where the melt pool temperature is hottest) within the physical limitations of the setup, this culminated in an ovular spot size of 2.2 mm × 1.6 mm. The thermal gradient of all samples was calculated using the simplified method outlined by Bermingham et al. [30]. An emissivity value of 0.36 was extrapolated from existing literature for liquid titanium [40]. The average melt pool temperature measured was used for the calculation and error calculated considering standard error [41] and instrumentation error of 0.3% as specified by the manufacturer throughout.

Deposition was monitored using a Xiris XVC-1100 welding process camera to ensure process stability and a consistent 'droplet' feedstock transfer mode. To ensure high image quality the camera aperture was decreased to the manufacturers minimum and a rolling shutter mode with 10 μs exposure time selected. A Xiris 50 mm lens was used in conjunction with a Xiris UV filter and clear glass spatter protection window.

Two specimens were machined from the center of each deposit for metallurgical analysis. A 30 mm x 30 mm transverse longitudinal section, machined to the central plane and a transverse section to look at the cross-section of the deposit. All samples were mounted in conductive phenolic resin using a hot mounting press and mechanically polished using consecutive grades of SiC paper from 240 grit to 2000 grit, before a final polish using colloidal silica and oxalic acid and etched using Kroll's reagent for approximately 10 s. Electron backscatter diffraction (EBSD) analysis was conducted using a Thermo Scientific Apreo C FEG-SEM at 20kv accelerating voltage and 51 nA beam current with 15 μm step size and processed using Oxford Instruments AztecCrystal. As Ti-6Al-4V exhibits allotropic behaviour, a solid state β to α transformation occurs during cooling, therefore, the β phase cannot be directly observed at room temperature. The transformation follows Burger's orientation relationship (BOR) i.e. $\{110\}_\beta$ // $\{0001\}_\alpha$ and $< 111 >_\beta$ // $< 0001 >_\alpha$ [42], which allows prior-β-phase maps to be generated from the acquired room temperature α-phase data using parent grain reconstruction developed by Davies and Wynne [43,44], with up to 3° divergence from BOR considered as part of the same grain and up to a 2° misorientation from a particular variant accepted. Quantitative prior-β grain size data was captured automatically by Oxford Instruments Aztec Crystal software and reported using the equivalent circle diameter. A high resolution large area mapping Hirox RH-2000 microscope was used for optical microscopy at 50x magnification.

Microhardness measurements were conducted using a Innovatest Falcon 503 and Vickers hardness test. A 300 g load was selected with an indentation dwell time of 10 s and 0.5 mm spacing. A total of 48 measurements were taken along the central plane from the top to bottom of the longitudinal specimens post-polishing and EBSD data acquisition.

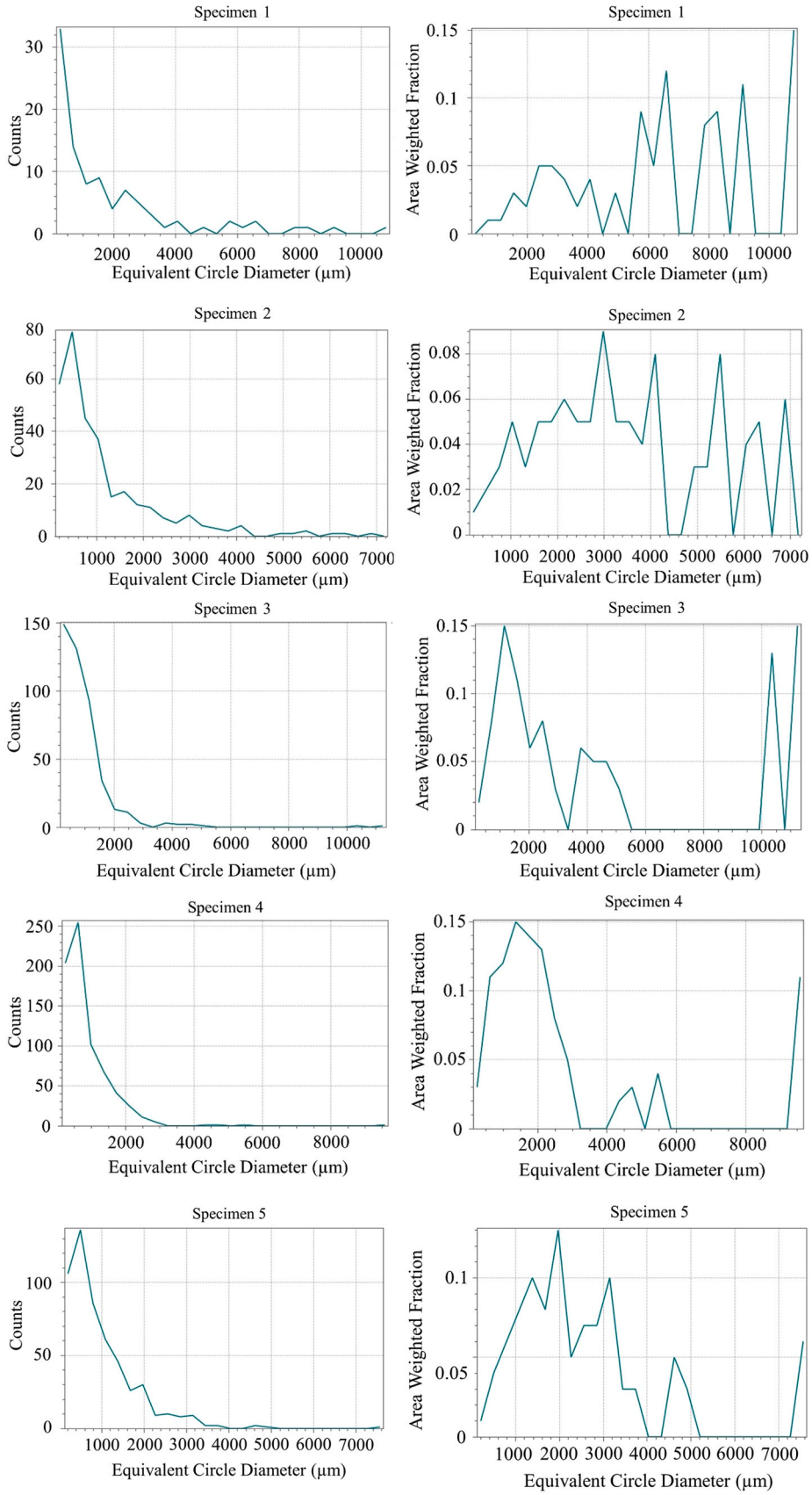


Fig. 9. Grain size distribution of specimens 1–5. (L) Number of counted grains (R) Area weighted distribution of grain size.

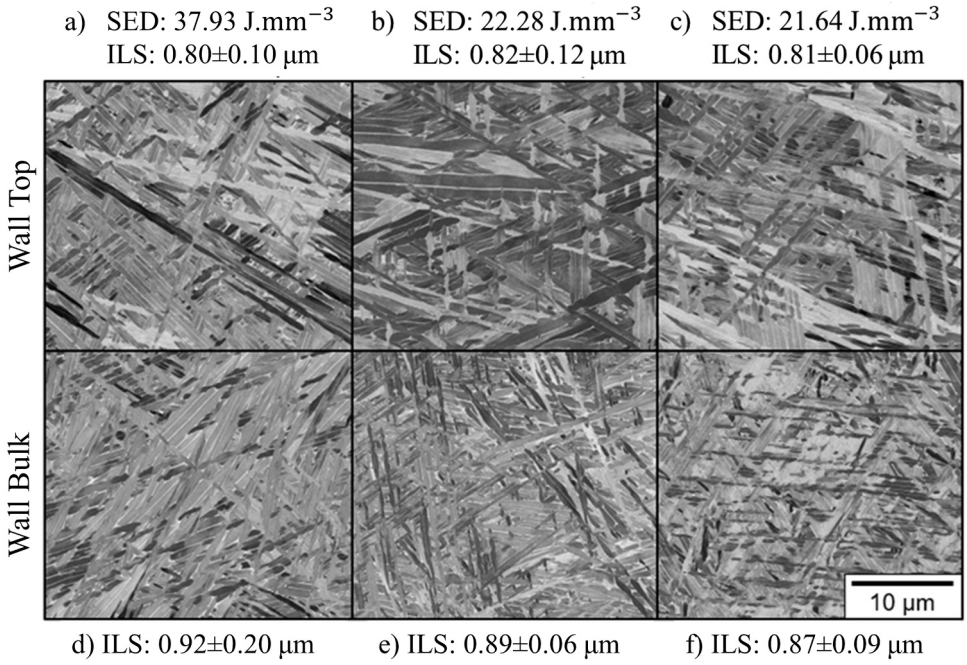


Fig. 10. Back-scattered electron images of α lamellar microstructure and measured ILS for Specimens 1,4 and 5 respectively a)-c) wall top, d)-f) wall bulk.

4. Results and discussion

The macrographs of the five longitudinal specimens may be observed in Fig. 2. There is a clear morphological change in the as-deposited prior-β grain structure. Fig. 2a) demonstrates a typical columnar grain structure, with the prior-β grains extending from the bottom of the deposit to the top. Moving through Figs. 2b) and 2c) the columnar grain structure begins to break down and refined grains begin to appear at the grain boundaries. Fig. 2d) and e) show a fully refined prior-β grain structure comprised of smaller refined grains. Evident in the macrographs presented in Fig. 2, is the effect of the thermal cycling innate to the WAAM process. This is demonstrated by the evidence of microstructural banding that is caused by the reheating of previously deposited material during subsequent deposition up to the β-transus temperature. The white banding appears as the alpha lamellar are coarsening [12] as they are essentially heat-treated and continue to grow. As the SED is reduced, the accompanying increase in layer height means the spacing between banding is becoming greater and less bands are visible in the specimens, improving homogeneity.

The columnar grain structure is caused by a combination of the high thermal gradient present during solidification and minimal solute segregation, minimising the amount of potential constitutional supercooling [22]. Aluminium and vanadium do not segregate sufficiently in titanium to generate a large liquidus temperature difference close to the solidification front. Reported partition coefficients for aluminium and vanadium range from 1.01 to 1.13 and 0.89 to 0.96 respectively [45,46]. With partition coefficients close to unity a significant change in thermal gradient is required to generate any constitutional supercooling. Typically, the nature of the WAAM process in the as-deposited condition exhibits high thermal gradients making this difficult to achieve which prevents homogenous nucleation or survival rate ahead of the solidification front, as is the case for the initial specimens. Growth occurred via an epitaxial growth mechanism, where solidifying atoms readily attach themselves to the pre-existing partially melted lattice of the previous grain, as this requires substantially less free energy than homogenous nucleation [47]. The resultant effect is the continuation of the previously deposited grain (columnar) in the same crystallographic orientation (texture). With the reduction in SED a morphological change in prior-β grain structure may be observed. As the arc energy, travel speed and alloy composition remain constant, this indicates that it is a response to a reduction in the thermal gradient A reduction in the thermal gradient generates constitutional supercooling, illustrated diagrammatically in Fig. 3, (note that for Ti-6Al-4V there is only a small change in T_L due to minimal solute partitioning and has been inflated diagrammatically for the purpose of explanation). Additionally, this highlights the difficulty in achieving prior-β grain refinement for Ti-6Al-4V, as the process window is minimal and difficult to obtain. The reduction in SED, thus thermal gradient, allows potential for nucleation ahead of the solidification front in the melt pool, increasing the survivability of randomly orientated nuclei and/or dendrite fragments from remelting and encouraging the potential for nuclei to activate [29]. These factors combined increase the opportunity for competitive growth and disruption to the epitaxial columnar grain structure, refining prior-β grain morphology and weakening texture.

Thermal gradients were calculated for each specimen using the simplified method outlined by Bermingham et al. [30]. This method required taking the difference between the peak temperature of the melt pool during deposition and solidification temperature and dividing over the height of the melt pool, thus providing an average linear thermal gradient approximation. These were determined to be: 528.4 ± 34.8 °C/mm, 351.1 ± 24.7 °C/mm, 283.5 ± 43.7 °C/mm, 208.0 ± 26.7 °C/mm and 196.6 ± 27.1 °C/mm for specimens 1–5 respectively. It can be deduced mathematically that the dominant variable for the calculation is the layer height during deposition. As may be observed in Fig. 4, the average layer height increased from 1.14 mm in specimen 1 to 2.48 mm in specimen 5, whilst the average peak temperature during deposition reduced from 2250 °C to 2130 °C. The average measured peak temperature remains consistent across specimens 1–2 and specimens 3–5, with an average temperature drop of ~100 °C occurring at specimen 3, which has a negligible effect on the thermal gradient calculated. Thus, the assumption that a reduction in SED would cool the melt pool is not unfounded but is not directly responsible for the drop in temperature as demonstrated by specimens 3–5, that have equivalent melt pool temperatures, instead it occurs in relation to the feedstock wire transfer mode.

As the SED is reduced there is a noticeable difference in the transfer mode (TM) of the feedstock material to the substrate from a small droplet to a large droplet. As described by Rios et. al. [37] the transfer



Fig. 11. Microhardness (HV0.3) measurements of specimens 1–5 - (1) 37.93 J.mm^{-3} (2) 30.39 J.mm^{-3} (3) 28.48 J.mm^{-3} (4) 22.28 J.mm^{-3} (5) 21.64 J.mm^{-3}.

mode during plasma arc welding with wire feedstock is categorised into four basic transfer modes: transfer mode 1 (TM1) the feedstock is in permanent contact with the melt pool with no interruptions; transfer mode 2 (TM2) is a droplet transfer mode where the droplet contact with the melt pool is approximately equivalent to the time required to grow a new droplet; transfer mode 3 (TM3) the growth time of the droplet is larger than the contact time and transfer mode 4 (TM4) growth time is significantly larger than the contact time and is reliant on the arc pressure to shear the droplet from the wire leading to erratic free fall. TM3 has a high potential to transform to TM4 and may be observed by the formation of spatter alongside the WAAM deposit. Generally, for stable deposition it is preferable that TM2 is maintained as it provides no risk of erratic droplet placement and a consistent frequency of droplet thus deposit shape, this can be controlled via the wire positioning within the arc and optimisation of deposition rate. During TM1, insufficiently melted feedstock has the possibility to fully penetrate the melt pool and skitter at the bottom of the melt leading to potential defects such as lack of fusion. TM4 should be avoided due to its erratic and unstable nature. Whilst TM3 is not ideal, in the case of this study no spatter was formed and droplet transfer and bead shape remained consistent when monitored via the processing camera. Therefore, in this controlled experimental environment both TM2 and TM3 can be referred to as stable.

The effects of feedstock TM on the heat flow and bead shape have been investigated extensively by Chen et. al. [48] and can be used to understand the reduction in peak temperature observed. A change in transfer mode is observed with the reduction in SED, from the two feed wires melting individually by small droplets (TM2) in specimens 1 and 2, before merging to create a singular larger droplet (TM3) in specimens 3–5. This may be observed in Fig. 5 for specimens 1–5 at the same randomly selected build height (~38 mm). It is important to note that whilst the larger droplet forms, the 'cold' wire does not penetrate the melt pool and a droplet transfer mode is maintained, therefore provides no benefits of melt pool agitation or introduction of negative thermal gradients to influence the grain structure. The ~100 ℃ drop is a consequence of the arc shading of the melt pool due to a reduction in the interaction between the arc and substrate caused by the larger droplet. The indication being that a reduction in the SED is not affecting the peak temperature observed during deposition. A similar effect is reported by Wang et al. [49], where the influence of wire diameter and deposition rate was considered, they demonstrated a large diameter wire (causing greater shading) led to less energy being delivered to the melt pool, measurable by the change in bead geometry in comparison to an equivalent deposition rate of a smaller diameter wire.

Additionally, it may be observed that the increase in average peak temperature uncertainty for specimens 3–5 is comparatively larger than specimens 1–2, this may also be attributed to the change in transfer mode and arc shading. The real-time pyrometric measurements recorded during deposition of specimens 1–5 for the respective layers

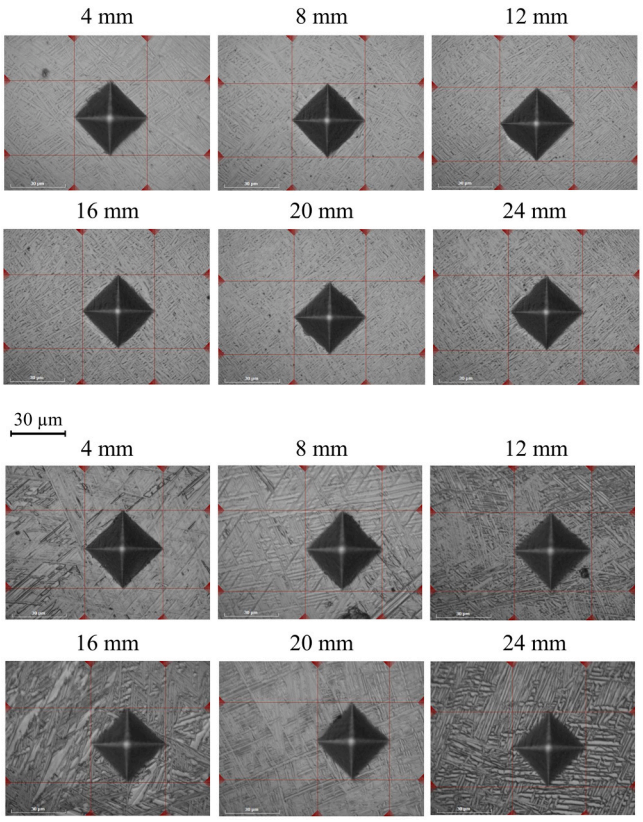


Fig. 12. Vickers hardness indentations showing localised microstructure of specimen 1 (columnar prior-β grains) and specimen 5 (refined prior-β grains) at 4 mm spacing below the top of the deposit.

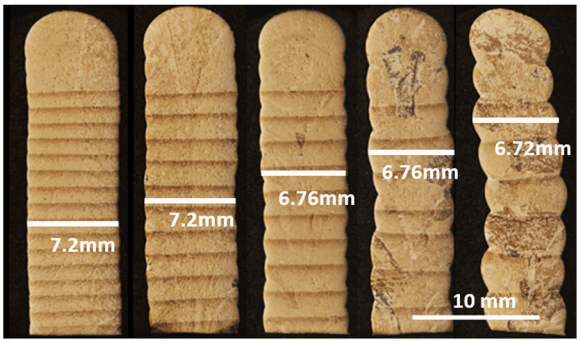


Fig. 13. Change in wall width and surface roughness as SED is reduced from 37.93 J.mm^{-3} (left), 30.39 J.mm^{-3}, 28.48 J.mm^{-3}, 22.28 J.mm^{-3}, 21.64 J.mm^{-3} (right).

observed in Fig. 5 is illustrated in Fig. 6. During TM2 for specimens 1–2 it may be observed that the variation in temperature is smaller than TM3. This is attributed to the aforementioned change in arc interaction with the melt pool due to arc shading. Whilst the droplet is growing larger during TM3 than TM2, this allows additional time for the melt pool to cool and prevents an equivalent amount of arc energy to interact with the melt pool surface, reducing the peak temperature. The point at which the droplet detaches, the arc is fully interacting with the melt pool at an equivalent rate to TM2 and heating the melt pool surface. Once the TM3 droplet size grows beyond the TM2 droplet detachment size, the melt pool begins to cool at faster rate once more. Taking into account the temperature peaks, it is possible to calculate the frequency of droplet transfer if necessary.

EBSD prior-β phase reconstructed maps of the 5 specimens may be observed in Fig. 7. Analysis of specimen 1 (Fig. 7a) highlights the texture of the columnar grain structure with weak misorientations of $< 5^{\circ}$ indicated by the similar shade of inverse pole figure (IPF) colouring. In this thermally stabilised region of material, heat primarily flows downwards by conduction and alongside the epitaxial growth mechanism, the grains have orientated themselves in to the 'easy' growth direction close to the build direction, $<100>_{\beta}$ in the case of BCC β-phase titanium. As the SED reduces, specimen 2 and 3 (Figs. 7b and 7c) shows evidence of the columnar structure beginning to break down with the introduction of randomly orientated refined grains appearing along the columnar grain boundaries. The texture is largely evident in the remaining columnar grains but shows evidence of weakening with the presence of high angle grain boundaries, indicated by the different (non-red) IPF colouring. In specimens 4 and 5 (Figs. 7d and 7e) a complete breakdown of the columnar structure to a refined one is indicated by the randomness of the IPF colouring and shape of the grains that may be observed. This is where grains have been prevented to grow via an epitaxial growth mechanism and instead are homogenously nucleated and competitively grow in randomly orientated directions.

The breakdown of texture as the SED reduces may be observed via the pole figures in Fig. 8. In specimen 1 and 2 (Figs. 8a and 8b) a distinctive concentration can be observed with a highly textured $<100>_{\beta}$ growth direction closest to the build direction (ND). This is not unexpected due to the epitaxial growth mechanism that dominates solidification. In specimen 3 (Fig. 8c), this texture begins to break down as grains are no longer solely developed by epitaxial growth but grown by new randomly orientated nuclei as well. In specimen 4 (Fig. 8d), it may be observed that the texture is no longer present with no distinctive areas of concentration, the implication being that at a reduced SED value it is possible to remove both the columnar prior-β grains and the crystallographic texture to produce grains via seemingly homogenous nucleation and competitive growth. In specimen 5 (Fig. 8e), qualitative examination of the prior-β grain reconstruction maps highlights a shift from the random orientation of the grains in specimen 4, implying there is an optimal value for SED to achieve refinement, to tilting towards the direction of the heat source travel direction. This is confirmed in the pole figure, with two concentrations appearing, tilted away from the ND to the working (WD) and transverse directions (TD). This appears to be evidence of the growth mechanism returning to an uncompetitive state, not unlike the typical columnar grain structure, albeit in the horizontal direction. It is known that preferential grain growth occurs along the maximum thermal gradient perpendicular to the solidification front [22, 30]. As the SED reduces, the layer height and therefore the melt pool shape is evolving, with solidification first occurring at the rear of the melt pool and seemingly provided a growth advantage. It is therefore implied that the melt pool shape may also play an important role in determining prior-β grain morphology and texture, therefore, this mechanism requires further investigation.

Post prior-β reconstruction, the grain size in each specimen was measured according to the equivalent circle diameter and the grain aspect ratio characterised to determine how close to an equiaxed structure was obtained during refinement (Table 3). However, given that the number of grains present in each specimen is relatively small, it is recommended that these results are indicative of the grain size and the grain size distribution should be consulted as reported in Fig. 9.

As expected when SED is reduced, it may be observed that the total number of grains increases and their size reduces in specimens 1–4, however, an unexpected decrease in the number of grains and increase in size is observed in specimen 5. Similarly, the aspect ratio decreases from specimens 1–4 until specimen 5 where an increase is also noted. This is particularly prevalent in the area weighted fraction of the grain size, in specimen 1, grains > 5000 µm dominate a large proportion of the grain structure, as the SED is reduced it may be observed that smaller grains account for an increasingly larger proportion of the measured area, by specimen 4 grains < 2000 µm dominate. However, during the deposition of specimen 5, there is an increase in grain size with a larger

proportion of grains growing between 2000 and 4000 μm despite a smaller SED, this is likely in relation to the horizontal tilt and return of seemingly preferential growth.

Fig. 10 presents the α microstructure as viewed from the top of the specimen and bulk material. The α microstructures observed show a predominantly Widmanstätten morphology where α plates overlap to create a basketweave effect, there is evidence of colony α, where several laths are grouped together in the same orientation and both elongated and fragmented α. Widmanstätten is the most common microstructure observed in Ti-6Al-4V deposited with WAAM and is determined by the cooling rate during solidification [22,30,32]. It may be observed that the reduction in the SED from specimen 1 to specimen 4 and 5, where refined prior-β grains exist, has no effect on the size (as calculated using the automated method by Zhao et al. [50]) of the α lamellar and thus indicates no change in cooling rate as expected, as the heat input has remained constant with little change in peak melt pool temperature being measured. There is an increase in the inter-lamellar spacing (ILS) of the bulk material as compared to the top material of the specimen, due to the coarsening effect previously mentioned, as a result of innate thermal cycling during WAAM heat treating the material. A smaller difference in the wall top and bulk ILS of specimens 4 and 5 may be observed compared to specimen 1 due to the reduction in the number of bands as a consequence of less thermal cycles spaced at larger intervals.

Due to the limited deposition size, it was not possible to extract tensile or fatigue specimens to characterize the mechanical performance with the reduction in SED and refinement of the prior-β grains. However, microhardness measurements of each specimen were conducted to give an indication of the mechanical performance and provide insight into other properties such as yield strength and wear resistance [51]. The average hardness for specimens 1–5 was found to be 346.17 Hv ± 11.19, 345.64 Hv± 9.82, 341.56 Hv ± 13.59, 328.45 Hv ± 17.79 and 325.32 Hv ± 16.31 respectively. The results of the microhardness tests are presented in Fig. 11. It may be observed that the average hardness of specimens 4 and 5, where prior-β grain refinement had occurred are 'softer' than the columnar dominant specimens, similarly a larger variance in specimens 4 and 5 was measured, with a minimum hardness measuring ~300 Hv reoccurring.

Given the similarity in ILS spacing, thus effective slip length, which has been demonstrated to be inversely proportional to hardness and strength [52] between columnar and refined specimens it was not expected that the value of hardness would diverge as significantly. Whilst further investigation is required to fully characterize the increase in hardness variation, initial investigation of the microstructures demonstrates varying α lamellar morphologies inside the refined prior-β grain specimens as opposed to a consistent Widmansttäten morphology seen across the columnar specimens. The significant difference in layer height as the SED undoubtedly leads to more complex thermal histories and cooling rates in the refined specimens as compared to the columnar specimens. The majority of the previous layer is beta annealed during the successive layer-upon-layer deposition and observed through the closer spacing of the coarsened α banding. Observed in Fig. 12 is the microhardness indentations made at an equal spacing below the top of the wall for the columnar prior-β grain specimen 1 and refined prior-β grain specimen 5. It is possible to observe a consistent Widmansttäten α microstructure versus various α morphologies in specimen 5, showing signs of Widmansttäten, acicular, fragmented lamellar, colony and elongated α. These changes in α morphology are most likely responsible for the variation in microhardness as it directly influences mechanical properties as seen in other studies [51–55]. Therefore, whilst the size of prior-β grains has reduced with SED, this introduces variability in the α microstructure morphology. To improve the homogeneity of the α microstructure it is possible to perform a β-anneal heat treatment [12,56], this allows the α microstructure to fully dissolve and using a controlled cooling rate, a uniform microstructure can be generated [57].

The reduction in the SED as a consequence of the increase in WFS, whilst beneficial to the prior-β grain structure, does present challenges during deposition, such as the change in TM, as discussed. To reduce the SED to the required value poses risk to deposition stability, as the limit of WFS can easily be reached without the introduction of multiple wire feeding. The consequence of maintaining the TS for variable WFS is the influence on the WFS/TS ratio, which effects bead geometry and thus forming quality. As the WFS/TS ratio is increased so too is the material deposited per unit length, leading to an increased layer height and lower forming quality, as the bead width is almost constant for a fixed TS, and consequently a larger surface roughness is generated [58]. In this experiment the effective wall width (EWW) was reduced by 20% from specimen 1–5 as surface roughness increased with the reduction in SED. The maximum wall width was reduced by the change in transfer mode from TM2 to TM3 due to the reduction in arc energy transferred to the substrate from arc shading [49]. As may be observed in Fig. 13, for specimens 1–2 the wall width is stable at 7.2 mm while TM2 is active and reduces to a minimum of 6.72 mm when TM3 is activated in specimens 3–5. The reduction in forming quality with SED in favour of a refined prior-β grain structure has the potential to reduce the productivity of the manufacturing processes as a sufficient bead overlap would be required to achieve homogenous deposits without lack of fusion defects.

5. Conclusions

The outcome of this study has shown that the as-deposited prior-β grain structure can be controlled during manufacturing without a reliance on post-processing or melt pool agitation. For a fixed heat input, by controlling the specific energy density (SED) of deposited material, the thermal gradient can be reduced to allow for epitaxial growth to be blocked and competitive dendritic growth to be achieved, with negligible effect on the inter-lamellar spacing (ILS), producing refined prior-β grains. However, whilst the ILS spacing remains consistent, the morphology of the α microstructure changes from a Widmansttäten dominant microstructure to including larger colony and fragmented α lamellar as SED is reduced. This influences the mechanical properties with a reduction in average Vickers hardness and larger variation in the refined prior-β grain specimens over their height as compared to the typical columnar prior-β grain specimens deposited using wire-direct energy deposition. An optimum SED exists before grains revert to a more dominant and previously unseen horizontally tilted grain growth. The change in SED does not appear to have considerable influence over the average peak melt pool temperature as compared to the feedstock transfer mode (TM) used during deposition which generates arc shading at high wire feed speed (WFS) rates. The reduction in SED leads to an unfavorable deposition geometry, however, highlighting that prior-β grain structure control is possible in the as-deposited condition without requiring post-processing.

The outcomes of this study can be summarised as follows:

1) For a fixed heat input, a reduction in the SED of deposited material can be used to refine the as-deposited prior-β grain structure and achieve close to an equiaxed morphology with minimal crystallographic texture.
2) When the SED of deposited material is reduced beyond an optimum, the morphology reverts to an uncompetitive horizontally tilted grain structure following the maximum thermal gradient from the solidification front at the rear of the melt pool.
3) The reduction in SED does not have a large effect on the peak melt pool temperature, which is instead determined by the TM of feedstock during deposition as a result of arc shading.
4) The reduction in SED provides greater ILS homogeneity between the top and bulk of the specimen due to a reduction in the α microstructural coarsening within a fixed volume as a result of increased layer height.
5) The reduction in SED has negligible effect on the ILS, however, changes the morphology of the α microstructure from

Widmansttäten dominant to including larger colony and fragmented α lamellar creating larger variation in the measured Vickers microhardness.

6) A reduction in the SED generates unfavorable surface roughness and reduction in effective wall width due to a decrease in the WFS/TS ratio, culminating in taller deposits with greater curvature.

In conclusion, the impact of this study is significant in laying the foundations for stable deposition of a localized prior-β grain structure in the as-deposited condition through simple modification of the solidification conditions via process control. This level of refinement has not previously been achieved in wire-direct energy deposition of Ti-6Al-4V without reliance on unstable deposition conditions, cold/hot-working, alloy modification or heat treatment. Further work is required to validate the SED hypothesis, in relation to differing process parameters and microstructural nuances that appear to occur in relation to the melt pool shape. However, this method of grain refinement proves promising in order to refine prior-β grains in the as-deposited condition through simple process control alone.

Funding Sources

This work was supported by the Engineering and Physical Science Research Council (EPSRC) [grant number: EP/R027218/1].

CRediT authorship contribution statement

Jialuo Ding: Writing – review & editing, Supervision, Resources, Project administration, Methodology, Funding acquisition, Conceptualization. **Stewart Williams:** Writing – review & editing, Supervision, Resources, Project administration, Methodology, Funding acquisition, Conceptualization. **James Christopher Julian Wainwright:** Writing – original draft, Visualization, Validation, Software, Project administration, Methodology, Investigation, Formal analysis, Data curation, Conceptualization.

Declaration of Competing Interest

The authors declare that they have no known competing financial interests or personal relationships that could have appeared to influence the work reported in this paper.

Data Availability

Data will be made available on request.

Acknowledgements

The authors would like to express their gratitude to the team at the Welding Engineering and Laser Processing Centre at Cranfield University. The authors would like to thank BAE Systems for sponsoring this research via funding through the EPSRC NEWAM programme (EP/R027218/1). The assistance from Dr Alec Davis generating the EBSD reconstructions. The authors would like to express their gratitude to John Thrower and Mark Allen in assisting with experimental setup and Steve Pope and Tracey Roberts for support polishing and etching samples.

References

[1] T. Pereira, J.V. Kennedy, J. Potgieter, A comparison of traditional manufacturing vs additive manufacturing, the best method for the job, Procedia Manuf. 30 (2019) 11–18, https://doi.org/10.1016/j.promfg.2019.02.003.

[2] S.W. Williams, F. Martina, A.C. Addison, J. Ding, G. Pardal, P. Colegrove, Wire + Arc Additive Manufacturing, Mater. Sci. Technol. 32 (2016) 641–647, https://doi.org/10.1179/1743284715Y.0000000073.

[3] Z. Pan, D. Ding, B. Wu, D. Cuiuri, H. Li, J. Norrish, Transactions on Intelligent Welding Manufacturing, Springer, Singapore, Singapore, 2018, https://doi.org/10.1007/978-981-10-5355-9.

[4] J.Z. Li, M.R. Alkahari, N.A.B. Rosli, R. Hasan, M.N. Sudin, F.R. Ramli, Review of wire arc additive manufacturing for 3D metal printing, Int. J. Autom. Technol. 13 (2019) 346–353, https://doi.org/10.20965/ijat.2019.p0346.

[5] A. Gisario, M. Kazarian, F. Martina, M. Mehrpouya, Metal additive manufacturing in the commercial aviation industry: a review, J. Manuf. Syst. 53 (2019) 124–149, https://doi.org/10.1016/j.jmsy.2019.08.005.

[6] A. Feier, I. Buta, C. Florica, L. Blaga, Optimization of Wire Arc Additive Manufacturing (WAAM) process for the production of mechanical components using a cnc machine, Materials 16 (2023), https://doi.org/10.3390/ma16010017.

[7] W.E. Frazier, Metal additive manufacturing: a review, J. Mater. Eng. Perform. 23 (2014) 1917–1928, https://doi.org/10.1007/s11665-014-0958-z.

[8] N. Jeyaprakash, A. Haile, M. Arunprasath, The parameters and equipments used in TIG welding: a review, Int J. Eng. Sci. (2015), 2319–1813.

[9] G. Marinelli, F. Martina, H. Lewtas, D. Hancock, S. Ganguly, S. Williams, Functionally graded structures of refractory metals by Wire Arc Additive Manufacturing, Sci. Technol. Weld. Join. 24 (2019) 495–503, https://doi.org/10.1080/13621718.2019.1586162.

[10] G. Lutjering, J.C. WIlliams. Titanium, second ed., Springer, Berlin, 2007.

[11] Z. Lin, K. Song, X. Yu, A review on wire and arc additive manufacturing of titanium alloy, J. Manuf. Process 70 (2021) 24–45, https://doi.org/10.1016/j.jmapro.2021.08.018.

[12] A. Ho, H. Zhao, J.W. Fellowes, F. Martina, A.E. Davis, P.B. Prangnell, On the origin of microstructural banding in Ti-6Al4V Wire-arc based high deposition rate additive manufacturing, Acta Mater. (2019), https://doi.org/10.1016/j.actamat.2018.12.038.

[13] J. Ding, P. Colegrove, F. Martina, S. Williams, R. Wiktorowicz, M.R. Palt, Development of a laminar flow local shielding device for Wire + Arc Additive Manufacture, J. Mater. Process Technol. (2015), https://doi.org/10.1016/j.jmatprotec.2015.07.005.

[14] A. Caballero, J. Ding, Y. Bandari, S. Williams, Oxidation of Ti-6Al-4V during wire and arc additive manufacture, 3D Print. Addit. Manuf. 6 (2019) 91–98, https://doi.org/10.1089/3dp.2017.0144.

[15] F. Wang, S. Williams, P. Colegrove, A.A. Antonysamy, Microstructure and mechanical properties of wire and arc additive manufactured Ti-6Al-4V, Metall. Mater. Trans. A 44 (2013) 968–977, https://doi.org/10.1007/s11661-012-1444-6.

[16] R. Kawalkar, H. Kumar Dubey, S.P. Lokhande, Wire Arc Additive Manufacturing: a brief review on advancements in addressing industrial challenges incurred with processing metallic alloys, Mater. Today Proc. 50 (2022) 1971–1978, https://doi.org/10.1016/j.matpr.2021.09.329.

[17] M. Qian, W. Xu, M. Brandt, H.P. Tang, Additive manufacturing and postprocessing of Ti-6Al-4V for superior mechanical properties, MRS Bull. 41 (2016) 775–784, https://doi.org/10.1557/mrs.2016.215.

[18] F. Martina, P.A. Colegrove, S.W. Williams, J. Meyer, Microstructure of interpass rolled Wire + Arc Additive Manufacturing Ti-6Al-4V components, Metall. Mater. Trans. A 46 (2015) 6103–6118, https://doi.org/10.1007/s11661-015-3172-1.

[19] J. Donoghue, A.A. Antonysamy, F. Martina, P.A. Colegrove, S.W. Williams, P. B. Prangnell, The effectiveness of combining rolling deformation with Wire–Arc Additive Manufacture on β-grain refinement and texture modification in Ti–6Al–4V, Mater. Charact. 114 (2016) 103–114, https://doi.org/10.1016/j.matchar.2016.02.001.

[20] J.R. Kennedy, A.E. Davis, A.E. Caballero, S. Williams, E.J. Pickering, P. B. Prangnell, The potential for grain refinement of Wire-Arc Additive Manufactured (WAAM) Ti-6Al-4V by ZrN and TiN inoculation, Addit. Manuf. 40 (2021), 101928, https://doi.org/10.1016/j.addma.2021.101928.

[21] J.R. Hönnige, A.E. Davis, A. Ho, J.R. Kennedy, L. Neto, P. Prangnell, S. Williams, The Effectiveness of Grain Refinement by Machine Hammer Peening in High Deposition Rate Wire-Arc AM Ti-6Al-4V, Met. Mater. Trans. A Phys. Met. Mater. Sci. 51 (2020) 3692–3703, https://doi.org/10.1007/s11661-020-05781-6.

[22] M.J. Bermingham, S.D. McDonald, M.S. Dargusch, D.H. StJohn, Grain-refinement mechanisms in titanium alloys, J. Mater. Res 23 (2008) 97–104, https://doi.org/10.1557/JMR.2008.0002.

[23] M.J. Bermingham, D. Kent, H. Zhan, D.H. Stjohn, M.S. Dargusch, Controlling the microstructure and properties of Wire Arc Additive Manufactured Ti-6Al-4V with trace boron additions, Acta Mater. 91 (2015) 289–303, https://doi.org/10.1016/j.actamat.2015.03.035.

[24] C.J. Todaro, M.A. Easton, D. Qiu, D. Zhang, M.J. Bermingham, E.W. Lui, M. Brandt, D.H. StJohn, M. Qian, Grain structure control during metal 3D printing by high-intensity ultrasound, Nat. Commun. 11 (2020) 1–9, https://doi.org/10.1038/s41467-019-13874-z.

[25] D. Yuan, S. Shao, C. Guo, F. Jiang, J. Wang, Grain refining of Ti-6Al-4V alloy fabricated by laser and wire additive manufacturing assisted with ultrasonic vibration, Ultrason Sonochem. 73 (2021), https://doi.org/10.1016/j.ultsonch.2021.105472.

[26] L. Neto, S. Williams, J. Ding, J. Hönnige, F. Martina, Mechanical properties enhancement of additive manufactured Ti-6Al-4V by machine hammer peening, Lect. Notes Mech. Eng. (2020) 121–132, https://doi.org/10.1007/978-981-15-0054-1_13.

[27] F.W.C. Farias, V.R. Duarte, I.O. Felice, J. da, C.P. Filho, N. Schell, E. Maawad, J. Y. Li, Y. Zhang, T.G. Santos, J.P. Oliveira, In situ interlayer hot forging arc plasma directed energy deposition of Inconel® 625: microstructure evolution during heat treatments, J. Alloy. Compd. 952 (2023), 170059, https://doi.org/10.1016/j.jallcom.2023.170059.

[28] V.R. Duarte, T.A. Rodrigues, N. Schell, R.M. Miranda, J.P. Oliveira, T.G. Santos, In-situ hot forging directed energy deposition-arc of CuAl8 alloy, Addit. Manuf. 55 (2022), https://doi.org/10.1016/j.addma.2022.102847.
[29] M. Bermingham, D. StJohn, M. Easton, L. Yuan, M. Dargusch, Revealing the Mechanisms of Grain Nucleation and Formation During Additive Manufacturing, Jom 72 (2020) 1065–1073, https://doi.org/10.1007/s11837-020-04019-5.
[30] M.J. Bermingham, D.H. StJohn, J. Krynen, S. Tedman-Jones, M.S. Dargusch, Promoting the columnar to equiaxed transition and grain refinement of titanium alloys during additive manufacturing, Acta Mater. 168 (2019) 261–274, https://doi.org/10.1016/j.actamat.2019.02.020.
[31] Q. Wu, J. Lu, C. Liu, H. Fan, X. Shi, J. Fu, S. Ma, Effect of molten pool size on microstructure and tensile properties of wire arc additive manufacturing of Ti-6Al-4V alloy, Materials 10 (2017) 1–11, https://doi.org/10.3390/ma10070749.
[32] P.A. Kobryn, S.L. Semiatin, Microstructure and texture evolution during solidification processing of Ti-6A1–4 V, J. Mater. Process Technol. 135 (2003) 330–339, https://doi.org/10.1016/S0924-0136(02)00865-8.
[33] D. Zhang, A. Prasad, M.J. Bermingham, C.J. Todaro, M.J. Benoit, M.N. Patel, D. Qiu, D.H. StJohn, M. Qian, M.A. Easton, Grain Refinement of Alloys in Fusion-Based Additive Manufacturing Processes, Met. Mater. Trans. A Phys. Met. Mater. Sci. 51 (2020) 4341–4359, https://doi.org/10.1007/s11661-020-05880-4.
[34] S. Sachi, M. Založnik, H. Combeau, C.A. Gandin, M. Gennesson, J. Demurger, M. Stoltz, I. Poitrault, Analysis of columnar-to-equiaxed transition experiment in lab scale steel casting by a multiphase model, IOP Conf. Ser. Mater. Sci. Eng. 529 (2019), https://doi.org/10.1088/1757-899X/529/1/012039.
[35] F. Martina, J. Mehnen, S.W. Williams, P. Colegrove, F. Wang, Investigation of the benefits of plasma deposition for the additive layer manufacture of Ti-6Al-4V, J. Mater. Process Technol. 212 (2012) 1377–1386, https://doi.org/10.1016/j.jmatprotec.2012.02.002.
[36] Z. Li, C. Liu, T. Xu, L. Ji, D. Wang, J. Lu, S. Ma, H. Fan, Reducing arc heat input and obtaining equiaxed grains by hot-wire method during arc additive manufacturing titanium alloy, Mater. Sci. Eng. A. 742 (2019) 287–294, https://doi.org/10.1016/j.msea.2018.11.022.
[37] S. Ríos, P.A. Colegrove, S.W. Williams, Metal transfer modes in plasma Wire + Arc Additive Manufacture, J. Mater. Process Technol. 264 (2019) 45–54, https://doi.org/10.1016/j.jmatprotec.2018.08.043.
[38] F. Wang, S. Williams, M. Rush, Morphology investigation on direct current pulsed gas tungsten arc welded additive layer manufactured Ti6Al4V alloy, Int. J. Adv. Manuf. Technol. 57 (2011) 597–603, https://doi.org/10.1007/s00170-011-3299-1.
[39] J. Wang, X. Lin, J. Li, A. Xue, F. Liu, W. Huang, E. Liang, A study on obtaining equiaxed prior-β grains of wire and arc additive manufactured Ti–6Al–4V, Mater. Sci. Eng.: A 772 (2020), 138703, https://doi.org/10.1016/j.msea.2019.138703.
[40] M. Mohr, R. Wunderlich, R. Novakovic, E. Ricci, H.J. Fecht, Precise measurements of thermophysical properties of liquid Ti–6Al–4V (Ti64) alloy on board the international space station, Adv. Eng. Mater. 22 (2020), https://doi.org/10.1002/adem.202000169.
[41] I. Farrance, R. Frenkel, Uncertainty of measurement: a review of the rules for calculating uncertainty components through functional relationships, Clin. Biochem Rev. 33 (2012) 49–75. ⟨http://www.ncbi.nlm.nih.gov/pubmed/22896744⟩.
[42] M. Humbert, N. Gey, The calculation of a parent grain orientation from inherited variants for approximate (b.c.c.-h.c.p.) orientation relations, J. Appl. Crystallogr 35 (2002) 401–405, https://doi.org/10.1107/S0021889802005824.
[43] P.S. Davies, An Investigation of Microstructure and Texture Evolution in the Near-a Titanium Alloy Timetal® 834, PhD Thesis, Univ. Sheff. (2009).
[44] P.S. Davies, B.P. Wynne, W.M. Rainforth, M.J. Thomas, P.L. Threadgill, Development of microstructure and crystallographic texture during stationary shoulder friction stir welding of Ti-6Al-4V, Met. Mater. Trans. A Phys. Met. Mater. Sci. 42 (2011) 2278–2289, https://doi.org/10.1007/s11661-011-0606-2.
[45] H. Mizukami, Y. Shirai, A. Kawakami, A. Mitchell, Solidification behavior of Ti-6Al-4V alloy, ISIJ Int. 60 (2020) 2455–2461, https://doi.org/10.2355/isijinternational.ISIJINT-2020-089.
[46] E. Doridot, S. Hans, A. Jardy, J.-P. Bellot, Industrial applications of modelling tools to simulate the PAMCHR casting and VAR process for Ti64, MATEC Web Conf. 321 (2020) 10011, https://doi.org/10.1051/matecconf/202032110011.
[47] S. Behavior, Weld Solidification, Weld integrity and performance, in: Weld Integrity and Performance, ASM International, 1997, pp. 3–21, https://doi.org/10.31399/asm.tb.wip.t65930003.
[48] X. Chen, C. Wang, J. Ding, P. Bridgeman, S. Williams, A three-dimensional wire-feeding model for heat and metal transfer, fluid flow, and bead shape in wire plasma arc additive manufacturing, J. Manuf. Process 83 (2022) 300–312, https://doi.org/10.1016/j.jmapro.2022.09.012.
[49] C. Wang, W. Suder, J. Ding, S. Williams, The effect of wire size on high deposition rate wire and plasma arc additive manufacture of Ti-6Al-4V, J. Mater. Process Technol. 288 (2021), https://doi.org/10.1016/j.jmatprotec.2020.116842.
[50] H. Zhao, A. Ho, A. Davis, A. Antonysamy, P. Prangnell, Automated image mapping and quantification of microstructure heterogeneity in additive manufactured Ti6Al4V, Mater. Charact. 147 (2019) 131–145, https://doi.org/10.1016/j.matchar.2018.10.027.
[51] J.S. Zuback, T. DebRoy, The hardness of additively manufactured alloys, Materials 11 (2018), https://doi.org/10.3390/ma11112070.
[52] G. Lütjering, Influence of processing on microstructure and mechanical properties of (α+β) titanium alloys, Mater. Sci. Eng.: A 243 (1998) 32–45, https://doi.org/10.1016/S0921-5093(97)00778-8.
[53] A. Shaikh, S. Kumar, A. Dawari, S. Kirwai, A. Patil, R. Singh, Effect of temperature and cooling rates on the α+β morphology of Ti-6Al-4V alloy, in: Procedia Structural Integrity, Elsevier B.V, 2019, pp. 782–789, https://doi.org/10.1016/j.prostr.2019.07.056.
[54] A. Dehghan-Manshadi, M.H. Reid, R.J. Dippenaar, in: J. Phys Conf Ser (Ed.), Effect of microstructural morphology on the mechanical properties of titanium alloys, Institute of Physics Publishing, 2010, https://doi.org/10.1088/1742-6596/240/1/012022.
[55] L. Vazquez, M.N. Rodriguez, I. Rodriguez, P. Alvarez, Influence of post-deposition heat treatments on the microstructure and tensile properties of ti-6al-4v parts manufactured by cmt-waam, Met. (Basel) 11 (2021), https://doi.org/10.3390/met11081161.
[56] E. Brandl, A. Schoberth, C. Leyens, Morphology, microstructure, and hardness of titanium (Ti-6Al-4V) blocks deposited by wire-feed additive layer manufacturing (ALM, Mater. Sci. Eng. A. 532 (2012) 295–307, https://doi.org/10.1016/j.msea.2011.10.095.
[57] E. Brandl, D. Greitemeier, Microstructure of additive layer manufactured Ti-6Al-4V after exceptional post heat treatments, Mater. Lett. 81 (2012) 84–87, https://doi.org/10.1016/j.matlet.2012.04.116.
[58] F. Martina, Investigation of methods to manipulate geometry, microstructure and mechanical properties in titanium large scale Wire + Arc Additive Manufacturing, Cranfield Univ. (2014).



https://dspace.org/

Refinement of Ti-6Al-4V prior- grain structure in the as-deposited condition via process control during wire-direct energy deposition

Wainwright, James; Williams, Stewart; Ding, Jialuo

2023-07-25
Elsevier
https://doi.org/10.1016/j.addma.2023.103712
Wainwright J, Williams S, Ding J. (2023) Refinement of Ti-6Al-4V prior- grain structure in the as-deposited condition via process control during wire-direct energy deposition. Additive Manufacturing, Volume 74, July 2023, Article number 103712

Downloaded from a DSpace repository. https://dspace.org/